

Oxygen left behind: Atmospheric Enrichment due to Fractionation in Sub-Neptunes using BOREAS*

MARILINA VALATSOU ,¹ CAROLINE DORN ,¹ PIERLOU MARTY,¹ AND JAMES E. OWEN ,²

¹*Institute for Particle Physics and Astrophysics, ETH Zurich, Wolfgang-Pauli-Strasse 27, 8093 Zurich Switzerland*

²*Astrophysics Group, Imperial College London, Prince Consort Road, London SW7 2AZ, UK*

ABSTRACT

The evolution of exoplanetary atmospheres is strongly influenced by atmospheric escape, particularly for close-in planets. Fractionation during atmospheric loss can preferentially remove lighter elements such as hydrogen, while retaining heavier species like oxygen. In this study, we investigate how and under what conditions hydrodynamic escape and chemical fractionation jointly shape the mass and composition of exoplanet atmospheres, especially for mixed H₂ + H₂O atmospheres. We develop BOREAS, a self-consistent mass loss model coupling a 1D Parker wind formulation with a mass-dependent fractionation scheme, which we apply across a range of planet masses, radii, equilibrium temperatures, and incident XUV fluxes, allowing us to track hydrogen and oxygen escape rates at different snapshots in time. We find that oxygen is efficiently retained over most of the parameter space. Significant oxygen loss occurs under high incident XUV fluxes, while at intermediate fluxes oxygen loss is largely confined to low-gravity planets. Where oxygen is retained, irradiation is too weak to drive significant escape of hydrogen and thus limiting atmospheric enrichment. By contrast, our model predicts that sub-Neptunes undergo substantial atmospheric enrichment over \sim 200 Myr when hydrogen escape is efficient and accompanied by partial oxygen entrainment. Notably, our results imply that sub-Neptunes near the radius valley can evolve into water-rich planets, in agreement with GJ 9827 d. Present-day water-rich atmospheres may have originated from water-poor envelopes under some conditions, highlighting the need to include chemical fractionation in evolution models. BOREAS is publicly available.

1. INTRODUCTION

The rapid increase in exoplanet detections over the past two decades has dramatically improved our understanding of planetary formation, evolution, and atmospheric dynamics. Among the most striking features of the exoplanet population is the wide diversity of atmospheric compositions, spanning from hydrogen-dominated primordial envelopes to This diversity is widely interpreted—especially for close-in planets—as the outcome of multiple evolutionary pathways, including primordial gas accretion, secondary atmosphere production through volatile outgassing, and atmospheric mass loss. The latter process is driven by intense stellar radiation, and can alter atmospheric composition, surface conditions, and long-term habitability (J. E. Owen 2019; F. Tian 2015). Volatile loss due to irradiation is also believed to have sculpted the terrestrial planets of our own Solar System, as demonstrated by isotopic and noble-gas signatures for Venus, Earth, and Mars (H. Lammer et al. 2008).

Observations of sub-Neptunes suggest a range of possibilities: some appear as steam worlds (C. Piaulet-Ghorayeb et al. 2024), while others may retain hydrogen-dominated envelopes, such as TOI-270 d (V. V. Eylen et al. 2021) and K2-18 b (N. Madhusudhan et al. 2023). Although there is considerable debate over whether sub-Neptunes are predominantly gas dwarfs or water worlds (J. L. Bean et al. 2021), recent global chemical equilibrium models indicate that all sub-Neptunes likely form water-poor, with bulk water mass fractions $< 2\%$, and initial water envelope mass fractions below 20 % (A. Werlen et al. 2025). Taken together, these results suggest that fractionated mass loss during a planet’s evolution may drive the atmospheric diversity of sub-Neptunes, since lighter species like hydrogen escape more readily than heavier ones, like oxygen. Here, we explore this hypothesis. Loss of volatiles such as water and hydrogen is crucial in determining whether a planet keeps its atmosphere or becomes a bare rocky world (R. Luger & R. Barnes 2015).

Hydrodynamic escape is a primary driver of atmospheric mass loss, particularly in young planetary systems, where high-energy stellar radiation ionizes atmospheric gases and powers outflows that can strip

* Released on February 13, 2026

hydrogen-rich envelopes and transform sub-Neptunes into super-Earths over geological timescales (E. D. Lopez et al. 2012; S. Jin et al. 2014; J. G. Rogers et al. 2021). The efficiency of this escape depends on stellar irradiation, planetary gravity, and atmospheric thermodynamics, with regimes such as energy- and recombination-limited escape setting mass loss rates (R. A. Murray-Clay et al. 2009; J. E. Owen & M. A. Alvarez 2015).

Both photoevaporation and core-powered mass loss shape the radius distribution of super-Earths and sub-Neptunes. Rather than competing, they act sequentially depending on system evolution and energy budget: photoevaporation is driven by stellar ultraviolet and X-ray (XUV) radiation (H. Lammer et al. 2003), while core-powered loss relies on residual cooling luminosity (S. Ginzburg et al. 2018). Which process dominates depends on the sonic point’s location relative to the XUV absorption depth. Population models reproduce the observed radius valley, highlighting photoevaporation as the primary sculptor, while core-powered loss remains important for weakly bound, highly irradiated planets (J. E. Owen & H. E. Schlichting 2024), though R. O. P. Loyd et al. (2020) find neither mechanism universally dominant. Here, we adopt a photoevaporation-dominated framework and do not explicitly model core-powered mass loss, although we can identify such outflows within our modeling framework.

In addition to mass loss, fractionation plays a key role in shaping atmospheric composition over time. For example, high-energy stellar radiation can dissociate the water molecules of a steam atmosphere into hydrogen and oxygen atoms, whose escape is governed by diffusive separation and hydrodynamic drag (K. J. Zahnle & J. F. Kasting 1986). Because hydrogen escapes more easily than oxygen, the atmosphere may become enriched in heavier elements—a trend supported by studies of transonic outflows in the Solar System (D. M. Hunten et al. 1987; K. Zahnle et al. 1990) and recent exoplanet models. C. Cherubim et al. (2024) showed that the degree of fractionation is highly dependent on the escape mechanism, with photoevaporation and core-powered loss producing distinct signatures in deuterium and helium. Preferential hydrogen loss can even cause abiotic O₂ buildup, a possible false biosignature as shown by , though other models suggest oxygen is largely dragged out with hydrogen (R. Burn et al. 2024). The application of fractionated loss at the population level C. Cherubim et al. (2025) has already revealed strong oxidation gradients and species-dependent loss signatures, demonstrating that coupled fractionation–escape modeling is feasible at scale. Yet, most models treat mass loss

and fractionation separately (C. Cherubim et al. 2025), leaving key questions unresolved. Full radiation hydrodynamic models could address this but remain computationally challenging for large populations.

Our semi-analytic hydrodynamic framework combines a generalized isothermal Parker-wind approach with self-consistent XUV penetration and recombination-limited physics to enable efficient exploration of a broad parameter space. Unlike simple energy-limited scaling models, where the XUV absorption radius is often assumed to match the planet’s radius, our method calculates the XUV radius; these are also the calculations that allow us to determine the transition from core-powered mass loss to photoevaporation. Additionally, it incorporates ionization-recombination equilibrium where appropriate, and enforces a matching condition for the sound speed and mass-loss rate without requiring full radiation-hydrodynamic simulations. At the same time, it simplifies certain aspects, such as the photo-dissociation efficiency and the detailed energy deposition, compared to full radiation hydrodynamic codes.

We explore simulations for a population of planets representative of the observed super-Earth and sub-Neptune population. Lastly, we benchmark our coupled model against existing mass loss rate estimates for well-characterized exoplanet systems (see Section 7.1). The detailed description of the photoevaporation framework is provided in Section 2, and the fractionation methodology is outlined in Section 3, with the results of applying it to super-Earth and sub-Neptune environments in Section 6.

2. ATMOSPHERIC ESCAPE MODEL

We build an XUV-driven photoevaporation model based on the modified Parker wind framework of J. E. Owen & H. E. Schlichting (2024). This approach accounts for both energy-limited and recombination-limited escape regimes, which depend on the atmospheric density and irradiation conditions. In the energy-limited regime, escape is driven by XUV heating, while in the recombination-limited regime, intense ionization forces hydrogen in a dense flow and radiative recombination becomes the main cooling mechanism. This recombination cooling thermostat sets the outflow to a temperature of approximately 10⁴ K and thus caps the mass loss rate. The regime classification and diagnostics follow J. E. Owen & H. E. Schlichting (2024). The mass-loss framework is coupled with a stellar XUV model that builds on I. Baraffe et al. (2015) and J. G. Rogers et al. (2021).

2.1. Stellar Irradiation Model

To calculate the received XUV flux F_{XUV} for a planet, we first estimate the star's XUV luminosity L_{XUV} . We assume that stars follow a characteristic ratio $L_{\text{XUV}}/L_{\text{bol}}$, which we interpolate as a function of stellar mass and age using the evolutionary tracks of I. Baraffe et al. (2015) and the empirical relations compiled in J. G. Rogers et al. (2021). Although this ratio varies weakly with stellar mass at fixed age, it captures the essential trend that younger and more massive stars emit higher XUV radiation than older or lower-mass stars. Once L_{XUV} is determined, the incident flux F_{XUV} at the planet's orbit is calculated directly from this luminosity and the orbital distance.

To establish the relevant orbital distance, we link the planet's equilibrium temperature T_{eq} to the star's bolometric luminosity L_{bol} using the standard planetary energy balance relation, which equates the absorbed stellar flux to the planet's thermal re-radiation. Specifically, we assume a Bond albedo $\alpha = 0.3$, a re-radiation fraction $\beta = 0.75$, and an emissivity $\epsilon = 1$. While these parameters are fixed for the models presented here, they remain configurable inputs to our framework for future analyses.

Finally, we adopt a heating efficiency of $\eta = 0.3$, which represents the fraction of absorbed XUV energy that effectively drives atmospheric escape rather than being radiated away from the planet. This value is consistent with prior photoevaporation models (J. E. Owen & H. E. Schlichting 2024) and is found to be appropriate for the low density planets we consider in this work (J. E. Owen & A. P. Jackson 2012; D. Kubyshkina et al. 2018).

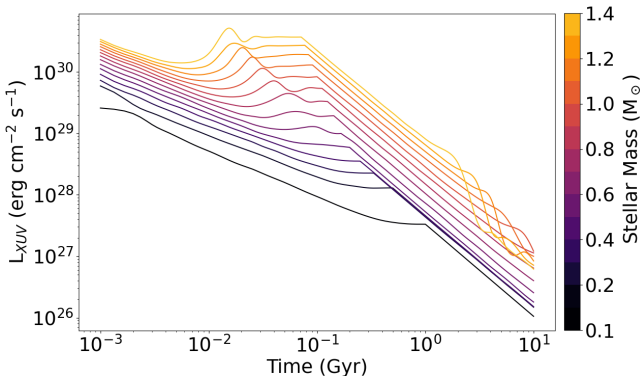


Figure 1. Time evolution of stellar XUV luminosity for stars of different masses, ranging from 0.1 to $1.4 M_{\odot}$.

2.2. Hydrodynamic Escape Approach

We model atmospheric outflow using a 1-dimensional, spherically symmetric, steady-state Parker wind model

following the methodology of J. E. Owen & H. E. Schlichting (2024). The general structure of the modeled atmosphere used to calculate mass loss is illustrated in Figure 2.

We approximate the radiative region above the radiative-convective boundary R_{rcb} as isothermal at the planet's T_{eq} , extending outward to the XUV absorption radius R_{XUV} . This treatment follows prior work on weakly luminous irradiated atmospheres (J. E. Owen & Y. Wu 2016, 2017). Beyond R_{XUV} , stellar XUV photons heat the gas to higher temperatures T_{outflow} , driving a photoevaporative outflow. The outflow remains subsonic from the base of the wind up to the sonic point at R_s , beyond which it transitions to supersonic expansion.

Within this structure, at smaller radii than R_{XUV} , we also define the transit radius of the planet R_{transit} . Finally, the Bondi radius R_B associated with a locally isothermal outflow is:

$$R_B = \frac{GM_p}{2c_s^2}, \quad (1)$$

where c_s is the local sound speed, and M_p is the planetary mass. For significant photoevaporation to occur in the sense of J. E. Owen & H. E. Schlichting (2024), we generally require $R_{\text{XUV}} < R_s < R_B$, such that XUV heating occurs inside the subsonic region and the wind can pass smoothly through the sonic point. In scenarios where $R_{\text{XUV}} > R_s$, mass loss can still occur; we treat these cases using the modified Parker-wind branch discussed in Appendix A.1. However, if $R_{\text{XUV}} > R_B$, this scenario would correspond to a core-powered mass loss regime. , we do not model it here.

2.3. Numerical Scheme and Density Structure

We discretize the radial domain (typically on a logarithmic grid) from R_p outward to several planetary radii, e.g., $5R_p$, covering the region affected by XUV-driven escape. The hydrodynamic solution is obtained by coupling an isothermal Parker wind above R_{XUV} to a hydrostatic, isothermal layer below R_{XUV} . For a given trial R_{XUV} , we determine an outflow sound speed c_s such that the resulting wind power is consistent with energy-limited heating. Specifically, the energy-limited mass-loss rate is

$$\dot{M}_{\text{EL}} = \eta F_{\text{XUV}} \frac{\pi R_{\text{XUV}}^3}{4G M_p}, \quad (2)$$

where F_{XUV} is the planet-averaged absorbed XUV flux (hence the factor of $1/4$). For fixed R_{XUV} , we solve for c_s using a root-finding procedure (Brent's method) such that the Parker-wind solution yields $\dot{M} = \dot{M}_{\text{EL}}$.

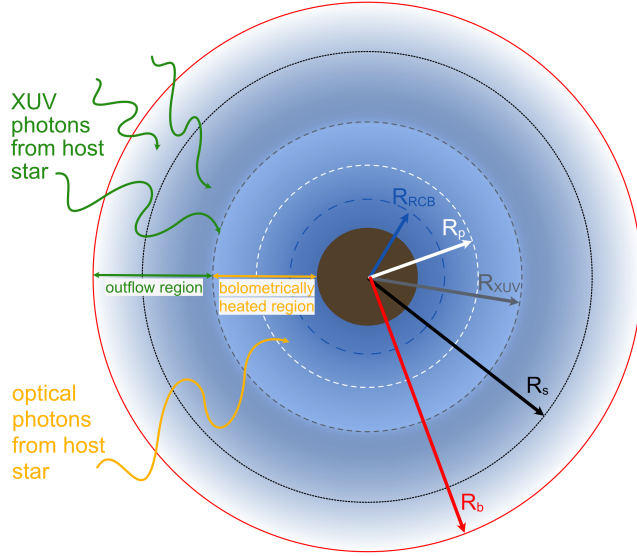


Figure 2. Schematic depiction of the model’s atmosphere, adapted from [J. E. Owen & H. E. Schlichting \(2024\)](#). For a planet undergoing significant photoevaporation, R_B lies outside R_{XUV} , and $R_s < R_B$.

The instantaneous mass-loss rate is computed from the wind base as

$$\dot{M} = 4\pi R_{XUV}^2 \rho(R_{XUV}) u(R_{XUV}), \quad (3)$$

where $u(R_{XUV})$ and $\rho(R_{XUV})$ are the velocity and density at the XUV base.

In our implementation, $\rho(R_{XUV})$ is set by requiring that the XUV optical depth above R_{XUV} be of order unity using a mass absorption coefficient χ_{XUV} (units $\text{cm}^2 \text{g}^{-1}$). For a given Parker-wind velocity field $u(r)$, we write the density profile up to an overall scale as $\rho(r) \propto (R_s/r)^2 (c_s/u(r))$ and compute the dimensionless column integral of the wind density profile

$$\tau_{\text{geom}}(R_{XUV}) \equiv \int_{R_{XUV}}^{\infty} \left(\frac{R_s}{r} \right)^2 \left(\frac{c_s}{u(r)} \right) dr, \quad (4)$$

so that the density normalization follows from the condition $\tau_{XUV} \sim 1$, yielding $\rho(R_{XUV}) = (\chi_{XUV} \tau_{\text{geom}})^{-1}$.

Finally, the physically consistent R_{XUV} is obtained by enforcing momentum balance across the transition from the hydrostatic layer to the photoevaporative flow, following [J. E. Owen & H. E. Schlichting \(2024\)](#). Concretely, for each trial R_{XUV} we compare (i) the hydrostatic pressure support implied by the bolometrically heated layer and (ii) the total momentum flux of the wind at launch. We scan over R_{XUV} and use root-finding to identify the R_{XUV} that satisfies the momentum-balance condition (Appendix A.1).

2.4. Escape Rate Evaluation and Regime Classification

Once an energy-limited solution is obtained, we evaluate whether the flow is instead recombination-limited using the diagnostic time-scale ratio ([J. E. Owen & H. E. Schlichting 2024](#)),

$$\mathcal{R}_t \equiv \frac{t_{\text{rec}}}{t_{\text{flow}}} = \frac{t_{\text{rec}}}{R_{XUV}/u(R_{XUV})}, \quad (5)$$

where $t_{\text{flow}} \sim H/u(R_{XUV})$ is the local advection time at the XUV base, $t_{\text{rec}} \sim 1/(\alpha_{\text{rec}} n_e)$ is the hydrogen recombination time. In that case we fix the outflow sound speed to $c_s \simeq 1.2 \times 10^6 \text{ cm s}^{-1}$ (corresponding to $T \sim 10^4 \text{ K}$), re-solve for R_{XUV} using the recombination-limited closure, and adopt the resulting \dot{M} , R_{XUV} , and c_s as our recombination-limited solution, as indicated in the flowchart in Appendix C, Figure 9.

3. ATMOSPHERIC FRACTIONATION APPROACH

We couple the hydrodynamic escape model to a diffusion–drag fractionation framework originally developed for elemental and isotopic escape in terrestrial Solar System atmospheres (Venus, Earth, Mars) ([K. J. Zahnle & J. F. Kasting 1986](#); [D. M. Hunten et al. 1987](#)), and implement it in the multi-species form described by [P. Odert et al. \(2018\)](#). In this work, we apply this approach specifically to hydrogen–oxygen fractionation in dissociated steam atmospheres and mixed $\text{H}_2 + \text{H}_2\text{O}$ atmospheres. For any mixture, we assume complete dissociation of the major molecular reservoirs at and above R_{XUV} and therefore treat the escaping gas as an atomic mixture. In the present implementation, we neglect helium as an explicit third species in the fractionation network. Our two-component treatment does not resolve the homopause explicitly and assumes that eddy diffusion is sufficiently strong to maintain a well-mixed composition up to the base of the wind.

Because heavier species are less readily accelerated by hydrodynamic flows, the escaping gas composition may deviate from the atmospheric bulk composition. In our case, hydrogen (the light species) escapes more efficiently, whereas oxygen (the heavy species) may remain partially gravitationally bound, especially on planets with deep gravitational potential ([K. J. Zahnle & J. F. Kasting 1986](#); [D. M. Hunten et al. 1987](#)). During episodes of significant atmospheric loss, this differential escape can alter the atmospheric composition and increase the O/H ratio in the remaining atmosphere. This directly affects the mean molecular weight of the escaping gas μ_{outflow} , which in turn influences key hydrodynamic escape quantities (e.g., density structure and the location of R_{XUV} through the XUV optical depth condition). To capture this feedback, our model embeds the

fractionation calculation within the main iteration loop for mass loss, ensuring that composition and outflow dynamics are solved jointly rather than in post-processing. The convergence procedure is detailed in Section 4.

3.1. Fractionation Factor and Flux Partitioning

Within each hydrodynamic iteration step, the mass-loss solver returns $(R_{\text{XUV}}, c_s, \dot{M})$ and thus a total mass flux at the wind base,

$$F_{\text{mass}} \equiv \frac{\dot{M}}{4\pi R_{\text{XUV}}^2} \quad [\text{g cm}^{-2} \text{s}^{-1}]. \quad (6)$$

We partition F_{mass} into *number* fluxes ϕ_{H} and ϕ_{O} (units $\text{cm}^{-2} \text{s}^{-1}$) for atomic hydrogen and oxygen in the escaping mixture. Defining the reservoir number ratio at the wind base as

$$f_{\text{O}} \equiv \left(\frac{n_{\text{O}}}{n_{\text{H}}} \right)_{\text{reservoir}}, \quad (7)$$

we solve for an oxygen entrainment (fractionation) factor $x_{\text{O}} \in [0, 1]$ such that the escaping oxygen number flux is

$$\phi_{\text{O}} = \phi_{\text{H}} f_{\text{O}} x_{\text{O}}. \quad (8)$$

Physically, x_{O} encodes the competition between gravitational settling and diffusive drag by hydrogen (Appendix B.1). When gravitational settling dominates, oxygen is inefficiently dragged and $x_{\text{O}} \ll 1$; when drag dominates, oxygen is efficiently entrained and $x_{\text{O}} \rightarrow 1$.

The hydrogen number flux ϕ_{H} is set by mass-flux conservation. Writing the total mass flux in terms of number fluxes,

$$F_{\text{mass}} = m_{\text{H}}\phi_{\text{H}} + m_{\text{O}}\phi_{\text{O}}, \quad (9)$$

and substituting $\phi_{\text{O}} = \phi_{\text{H}} f_{\text{O}} x_{\text{O}}$ gives

$$\phi_{\text{H}} = \frac{F_{\text{mass}}}{m_{\text{H}} + m_{\text{O}} f_{\text{O}} x_{\text{O}}}, \quad (10)$$

Because x_{O} depends on ϕ_{H} through the diffusion–drag relations, we solve these equations by fixed-point iteration on x_{O} (or equivalently on ϕ_{O}), which converges rapidly for the regimes explored here.

Finally, we compute the mean molecular weight of the escaping H–O mixture (in hydrogen-mass units) as

$$\mu_{\text{outflow}} = \frac{\phi_{\text{H}} m_{\text{H}} + \phi_{\text{O}} m_{\text{O}}}{m_{\text{H}}(\phi_{\text{H}} + \phi_{\text{O}})}. \quad (11)$$

This μ_{outflow} is fed back into the hydrodynamic solution in the coupled iteration described next.

4. NUMERICAL SOLUTION FOR COUPLED MASS LOSS AND FRACTIONATION

We solve the coupled hydrodynamic mass loss and hydrogen–oxygen fractionation problem using a self-consistent iterative scheme. In our framework, the fractionated composition modifies the mean molecular weight μ_{outflow} of the escaping gas and also modifies the XUV absorption through the mass absorption coefficient χ_{XUV} evaluated for an atomic mixture at R_{XUV} . We therefore iterate hydrodynamics and fractionation jointly until convergence.

For a single planet, the coupled iteration proceeds as follows:

1. Initialize the outflow mean molecular weight μ_{outflow} from the fully dissociated reservoir composition (Section 5.2), and construct an initial atomic mixture at R_{XUV} for evaluating χ_{XUV} .
2. For the current $(\mu_{\text{outflow}}, \chi_{\text{XUV}})$, solve the hydrodynamic escape problem to obtain $(\dot{M}, c_s, R_s, R_{\text{XUV}})$ (Section 2.3). We first compute the energy-limited solution and then, if the time-scale criterion indicates rapid recombination, adopt a recombination-limited solution (Section 2.4).
3. Compute the outflow temperature used in the fractionation step. In the recombination-limited regime we set $T_{\text{outflow}} = 10^4 \text{ K}$, consistent with the recombination thermostat; otherwise we map T_{outflow} from $(c_s, \mu_{\text{outflow}})$ via $T_{\text{outflow}} = c_s^2 m_{\text{H}} \mu_{\text{outflow}} / k_{\text{B}}$.
4. Using $(R_{\text{XUV}}, T_{\text{outflow}}, \dot{M})$, compute the total mass flux F_{mass} and apply the fractionation solver to obtain the number fluxes ϕ_s and entrainment factors x_s (Section 3.1).
5. Update the atomic mixture at R_{XUV} from the escaping fluxes, $y_s \equiv \phi_s / \sum_s \phi_s$, and recompute μ_{outflow} from the flux-weighted mixture:

$$\mu_{\text{outflow}} = \frac{\sum_s \phi_s m_s}{m_{\text{H}} \sum_s \phi_s}. \quad (12)$$

6. Check convergence of μ_{outflow} . The iteration terminates when $|\mu_{\text{outflow,new}} - \mu_{\text{outflow,old}}| / \mu_{\text{outflow,old}} < 10^{-5}$. Otherwise, return to step 2.

A schematic overview of these steps is provided in the Appendix C, Figure 9.

5. MODEL PARAMETERS AND ASSUMPTIONS

Here, we summarize the key physical parameters, opacities, and coefficients adopted throughout our framework, as well as the primary assumptions under our numerical implementation. These choices form the foundation for all hydrodynamic and fractionation calculations.

5.1. Recombination, Diffusion, and Opacity Coefficients

The recombination coefficient, governing the balance of ionization and recombination in the outflow region, is set to $\alpha_{\text{rec}} = 2.6 \times 10^{-13} \text{ cm}^3/\text{s}$ (P. J. Storey & D. G. Hummer 1995; D. E. Osterbrock & G. J. Ferland 2006).

The absorption of XUV photons is parameterized by atomic photoabsorption cross-sections $\sigma_{\text{XUV},\text{H}}$ and $\sigma_{\text{XUV},\text{O}}$, which we combine into a mass absorption coefficient χ_{XUV} (units $\text{cm}^2 \text{ g}^{-1}$) at R_{XUV} . We adopt $\sigma_{\text{XUV}} \approx 1.89 \times 10^{-18} \text{ cm}^2$ for both atomic hydrogen (R. A. Murray-Clay et al. 2009) and oxygen, given their nearly identical photoionization cross-sections (D. A. Verner et al. 1996), assuming monochromatic XUV spectrum at $h\nu = 20 \text{ eV}$. For an atomic H–O mixture with number fractions y_{H} and y_{O} , we compute

$$\chi_{\text{XUV}} = \frac{y_{\text{H}}\sigma_{\text{XUV},\text{H}} + y_{\text{O}}\sigma_{\text{XUV},\text{O}}}{\mu_{\text{outflow}} m_{\text{H}}}, \quad (13)$$

where μ_{outflow} is the mean particle mass in units of m_{H} . In the coupled iteration, $(y_{\text{H}}, y_{\text{O}})$ are updated from the escaping fluxes via $y_s = \phi_s / (\phi_{\text{H}} + \phi_{\text{O}})$.

The opacity to outgoing thermal radiation, which characterizes radiative transfer through the escaping atmosphere, is taken as $\kappa_{\text{H/He}} \approx 0.01 \text{ cm}^2 \text{ g}^{-1}$ for a pure H/He atmosphere (e.g., S. Seager 2010; J. E. Owen & Y. Wu 2017), and $\kappa_{\text{H}_2\text{O}} \approx 1 \text{ cm}^2 \text{ g}^{-1}$ for a pure steam atmosphere (e.g., T. Guillot 2010; S. Seager 2010). For mixed cases we use an approximation: we perform a weighted interpolation of the pure-component opacities, e.g., a mixture of 10% H_2O by mass with background hydrogen yields $\kappa_{\text{H}_2, \text{H}_2\text{O}} \approx 0.11 \text{ cm}^2 \text{ g}^{-1}$.

We also adopt the binary diffusion coefficient for oxygen in hydrogen, $b_i = 4.8 \times 10^{17} T_{\text{outflow}}^{0.75} \text{ cm}^{-1} \text{ s}^{-1}$, following Table 1 from K. J. Zahnle & J. F. Kasting (1986). This coefficient is used in the fractionation calculations and reflects the drag force exerted on oxygen atoms by a hydrogen background at temperature T_{outflow} (see Appendix B.1).

5.2. Mean Molecular Weight and Atmospheric Composition

Below R_{XUV} , we assume the atmosphere is well mixed and reflects its bulk molecular composition as shown in

Figure 2. The bolometric mean molecular weight μ_{bolo} is computed from the molecular reservoir mass fractions and is used to evaluate the isothermal sound speed in the radiative layer, $c_{s,\text{bolo}} = \sqrt{k_{\text{B}} T_{\text{eq}} / (\mu_{\text{bolo}} m_{\text{H}})}$. In this work, the mean molecular weight ranges from 2.35 g mol^{-1} (pure primordial H/He gas) to 18 g mol^{-1} (pure H_2O steam atmosphere).

Above R_{XUV} , we assume full dissociation of the molecular reservoirs and treat the escaping gas as an atomic mixture. The outflow mean molecular weight μ_{outflow} is defined as the mean particle mass in units of m_{H} . For a pure steam atmosphere, dissociation yields two H atoms and one O atom per H_2O molecule, giving $\mu_{\text{outflow}} = 6$. In mixed $\text{H}_2 + \text{H}_2\text{O}$ envelopes, μ_{outflow} lies between $\simeq 1$ (hydrogen-dominated) and 6 (steam-dominated), and is updated self-consistently from the escaping fluxes in the coupled iteration (Section 4). For example, in a 90% $\text{H}_2 + 10\% \text{H}_2\text{O}$ envelope, dissociation yields an approximate $\mu \approx 1.09 \text{ g/mol}$.

5.3. Planetary Models and Input Parameters

We apply our coupled mass loss and fractionation model to the following scenarios:

1. Young super-Earths and sub-Neptunes, with the goal of determining changes in atmospheric properties over time.
2. Evolved super-Earths and sub-Neptunes, with the goal of determining mass loss rates and the fractionation efficiency for various planet properties.

Planetary radii are computed using a self-consistent interior structure model after C. Dorn et al. (2015, 2017), with recent updates from H. Luo et al. (2024). The model assumes an iron-rich core, a rocky mantle, and, where applicable, a surface ocean or an extended volatile envelope. Deep interior profiles are assumed to be adiabatic. The thermodynamic state of the convective interior is set by the intrinsic luminosity, following the thermal evolution prescriptions of C. Mordasini (2020).

For sub-Neptunes, we model planets with masses of $2\text{--}15 M_{\oplus}$. We generate both inflated, young planets initialized at an age of $\sim 100 \text{ Myr}$, as well as more compact, thermally evolved planets. For the young cases, the planet intrinsic luminosity is calculated following the luminosity model of (C. Mordasini 2020) and is a function of planet mass, atmospheric mass fraction, and planet age. For evolved sub-Neptunes, we instead prescribe a fixed intrinsic luminosity of $L_{\text{int}} = 10^{21} \text{ erg s}^{-1}$, representative of late-time cooling states. These planets are assigned equilibrium temperatures of 300 K and 1000 K to explore a range of irradiation environments,

and envelope compositions including atmospheres (3% by planet mass) made up of either pure H/He, or H₂ containing 10–90% water by atmospheric mass.

- Young sub-Neptunes: approx. $2.24 - 2.86 R_{\oplus}$ at 400 K, and $2.77 - 3.54 R_{\oplus}$ at 2000 K.
- Evolved sub-Neptunes: approx. $1.35 - 2.68 R_{\oplus}$ at 400 K, and $1.53 - 3.36 R_{\oplus}$ at 2000 K.

For super-Earths, we model rocky planets with masses of $1-10 M_{\oplus}$, with thin (3% by mass, following J. G. Rogers et al. (2024)) volatile water layers overlying a differentiated interior. We adopt equilibrium temperatures of 400 K and 2000 K to represent cooler, thermally evolved planets and hotter, more strongly irradiated planets, respectively.

6. RESULTS

6.1. Mass Loss and Global Oxygen Fractionation Trends

In this section we present results for evolved super-Earths and sub-Neptunes, mapping how instantaneous mass loss rates and oxygen retention vary across planetary mass, atmospheric composition, and irradiation, and identifying where fractionation becomes important and where oxygen is efficiently retained.

Figure 3 shows the total atmospheric mass loss rates depending on incident XUV fluxes for different planetary masses, T_{eq} , and envelope compositions. Incident XUV fluxes are consistent with the corresponding T_{eq} . In general, 1) lower mass planets have less strong gravity and thus lose more atmospheric mass for a given F_{XUV} , 2) planets with higher T_{eq} have higher mass loss rates than cooler planets with similar mass and incident F_{XUV} , due to their inflated radii. It is clear that F_{XUV} is the main driving factor for total mass loss rates.

F_{XUV} is also the main factor that determines whether oxygen loss is significant or suppressed, illustrated in Figure 4 for both super-Earths and evolved sub-Neptunes. Oxygen loss is shown as the instantaneous oxygen fractionation factor x_O , ranging from 0 (no oxygen loss) to 1 (no fractionation). It directly relates to the escape flux ϕ_O , as shown in Appendix B.1, Eq. B9. Increasing F_{XUV} leads to a sharp transition between two regimes: one in which no oxygen is dragged along ($x_O = 0$, gray regions) and another in which (close to) the bulk composition is lost ($x_O \approx 1$, yellow regions). Compared to the influence of F_{XUV} , planetary mass and radius have secondary effects. A closer look at Figure 4 shows that:

1. Super-Earths (top panels) at $T_{\text{eq}} = 2,000$ K span both energy-limited and recombination-limited es-

cape, with the transition between regimes depending on F_{XUV} . High oxygen loss in the mass regime may occur for $F_{\text{XUV}} \gtrsim 5 \times 10^3 \text{ erg cm}^{-2} \text{ s}^{-1}$, regardless of planet mass, but more massive planets ($M_p \gtrsim 4 M_{\oplus}$) lose significant amounts of oxygen ($x_O \geq 0.1$) for $F_{\text{XUV}} \gtrsim 10^4 \text{ erg cm}^{-2} \text{ s}^{-1}$. Under the high T_{eq} and irradiation environment of these super-Earths, the entire space of modeled radii correlates with efficient oxygen loss. For the low end of XUV fluxes, smaller planets lose less oxygen (color gradient) or no oxygen (gray points). Cooler super-Earths at $T_{\text{eq}} = 400$ K remain in the energy-limited regime with negligible oxygen escape, with the exception of a narrow low mass-high irradiation regime, confirming that F_{XUV} is the main controlling parameter for oxygen loss.

2. Sub-Neptunes (bottom panels) at $T_{\text{eq}} = 1,000$ K, similarly to the warm super-Earths, require high F_{XUV} , both in the mass and radius regimes, to enable oxygen escape. Significant oxygen loss appears for $F_{\text{XUV}} \gtrsim 10^3$ for most masses and radii, with more extreme thresholds ($F_{\text{XUV}} \gtrsim 10^4$) needed for planets with masses over $10 M_{\oplus}$. At masses below $\sim 6 M_{\oplus}$, lower F_{XUV} may drive oxygen loss and escape occurs under energy-limited conditions. The most inflated warm sub-Neptunes show oxygen loss under all irradiation environments. Similar to super-Earths, cooler sub-Neptunes at $T_{\text{eq}} = 300$ K show no significant oxygen loss, regardless of radius or mass, reaffirming that high XUV flux is a prerequisite for fractionation to matter. It is important to note that for this category of planets, significant oxygen loss is likely to coincide with the epoch when these planets lose the bulk of their envelopes.

To further examine oxygen’s contribution to the total escape flow, a direct diagnostic is the atomic ratio O/H escape flux. Figure 5 presents this ratio for all simulated planets. Dashed lines in the figure indicate the mixing-limited maximum O/H ratio corresponding to each atmosphere composition (10–90% water for sub-Neptunes, 100% water for super-Earths, with, e.g., a O/H ratio of 0.5 for pure H₂O), representing the upper limit where no fractionation happens and oxygen escapes at the same rate as its atmospheric abundance. Calculated escape flux ratios \dot{N}_O/\dot{N}_H are always lower than the mixing-limited ratios by construction, and lower escape flux ratios imply stronger fractionation. Values of $\dot{N}_O/\dot{N}_H = 0$ correspond to cases where no oxygen is lost, with $x_O = 0$. For cases where x_O approaches unity, the escape flux ratios closely approach the mixing-

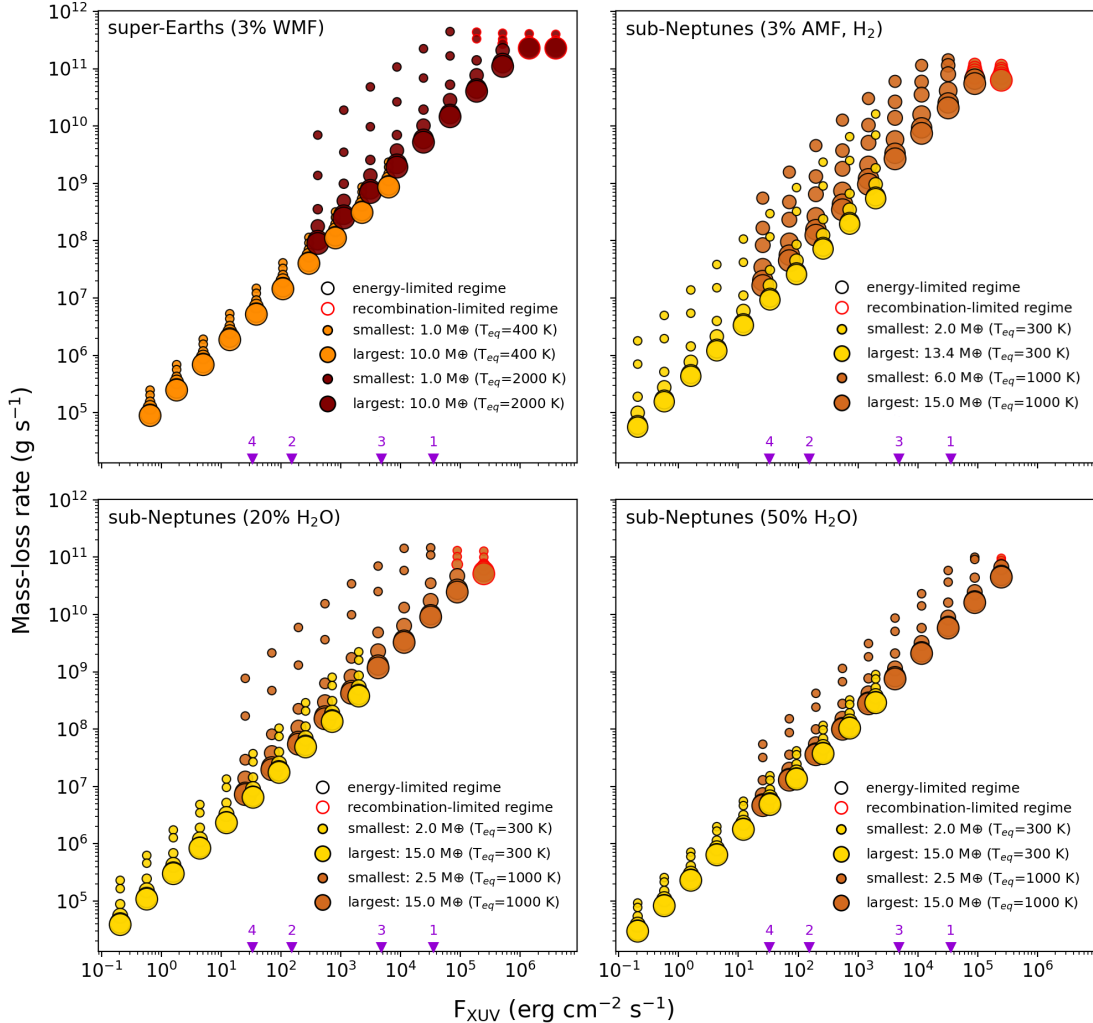


Figure 3. Mass loss rate \dot{M} as a function of F_{XUV} for a range of planetary compositions and envelope structures. Each panel shows results for a different atmospheric configuration: (top left) super-Earths with 3% water mass fraction (WMF) and a purely steam H₂O atmosphere; (top right) sub-Neptunes with 3% atmospheric mass fraction (AMF) in H/He; (bottom left) sub-Neptunes with 3% AMF in H₂ and 10% envelope WMF; (bottom right) sub-Neptunes with 3% AMF and 50% envelope WMF. Each point corresponds to a specific model with varying T_{eq} and planet mass. Marker size reflects planetary mass, where the minimum, maximum, and few cases in between are plotted. Color denotes equilibrium temperature (from yellow to maroon with increasing T_{eq}), and red point edges flag the recombination-limited regime. The purple indicators represent the XUV fluxes of certain scenarios and are there for context; indicators 1) and 2) correspond to the flux an Earth-like planet receives around a Sun-like star at an orbital period of 10 days, at 50 Myr and 5 Gyr, respectively; 3) and 4) are similar to 1) and 2) but for an M-star of mass $0.4M_{\odot}$. Across the parameter space, higher XUV flux and lower mass lead to increased \dot{M} .

limited ratios. We find that Lastly, consistent with H-dominated winds, planets with mixed H₂ + H₂O atmospheres exhibit systematically lower O/H ratios at a given hydrogen flux compared to pure steam super-Earths, because oxygen is always a trace component in a primarily hydrogen wind. This enhanced diffusive separation reduces drag on O atoms and further suppresses their escape.

6.2. Atmosphere evolution over time

In this second part, we apply our model to super-Earths and sub-Neptunes to determine how mass loss

and fractionation alter their atmospheric properties over time. We focus on the possible water depletion for super-Earths and atmospheric enrichment of young sub-Neptunes over a time span of 200 Myrs; this corresponds to the timespan after disk dispersal when XUV-driven mass loss is expected to be strongest (Figure 1).

While our model is designed to evaluate atmospheric escape and fractionation at fixed planetary snapshots, these instantaneous rates can offer valuable insight into the cumulative volatile loss experienced by a planet over time. To assess the broader implications of our results,

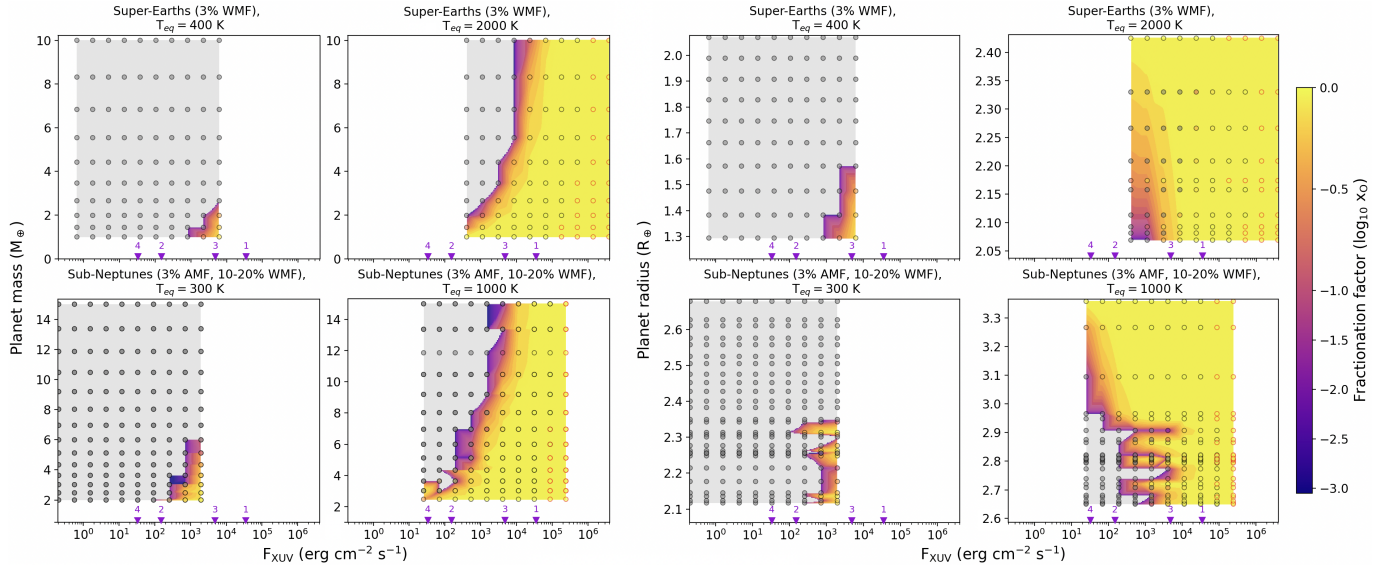


Figure 4. Oxygen fractionation factor map over planetary mass (left) and radius (right), and incident F_{XUV} , pooled across envelope compositions and T_{eq} . Gray shaded regions and scatter points show a fractionation factor for oxygen of 0 (no oxygen loss), while the colorbar shows increasing fractionation factors towards yellow colors. A fractionation factor of 1 means that oxygen is lost according to the mixing ratio (e.g., 1 oxygen atom per 2 hydrogen atoms in a pure steam atmosphere). Red point edges flag the recombination-limited regime.

we estimate the total water mass loss over 200 Myrs. Our estimates should be interpreted as upper bounds on potential water loss rather than precise evolutionary tracks. . A more complete treatment of water loss across time would require coupling radius evolution, thermal contraction, and stellar activity history, all of which would lower our estimates.

6.2.1. How much water can be lost from Super-Earths due to oxygen fractionation?

In order to estimate the maximum amount of water that can be lost over 200 Myrs from super-Earths with steam-dominated atmospheres (3% WMF), we convert oxygen escape fluxes to the cumulative water loss. In practice, each escaping oxygen atom is paired with two hydrogen atoms, consistent with H_2O stoichiometry. This yields the rate of water molecules lost over time, which we multiply by 200 Myr to obtain the total water loss in Earth oceans.

Figure 6 shows the cumulative oxygen loss, expressed in equivalent Earth oceans (EO) of H_2O as a function of incident XUV flux, as well as enrichment of oxygen in the remaining atmosphere due to preferential hydrogen loss in the bottom panel. This assumes instantaneous recombination of remaining hydrogen and oxygen into water and molecular oxygen. The result exhibit a threshold-dominated behavior controlled by whether oxygen is entrained in the escaping hydrogen flow, similar to Figure 5. For most planets at low irradiation levels ($F_{\text{XUV}} \lesssim 10^3 - 10^4 \text{ erg cm}^{-2} \text{ s}^{-1}$), oxygen

escape is suppressed ($\phi_{\text{O}} = 0$), resulting in negligible oxygen-equivalent-water loss despite ongoing hydrogen escape (middle panel). In this regime, oxygen is retained and oxygen-equivalent-water loss is effectively halted by diffusion-limited fractionation; here, we observe an atmospheric enrichment in the order of 2 % over the escape timescale (bottom panel).

At higher irradiation levels, a subset of planets transitions into a regime where oxygen becomes entrained and significant water loss occurs. For hot super-Earths ($T_{\text{eq}} = 2,000 \text{ K}$, shown in dark red), this transition typically occurs at $F_{\text{XUV}} \gtrsim 3 \cdot 10^2 - 10^3 \text{ erg cm}^{-2} \text{ s}^{-1}$, with oxygen loss increasing rapidly beyond this threshold. In these cases, cumulative losses of a few to hundreds of Earth oceans over 200 Myr are possible, and some planets are fully desiccated within this timescale (cross symbols). Cooler super-Earths ($T_{\text{eq}} = 400 \text{ K}$) rarely enter this regime and generally retain their oxygen-equivalent-water inventories across the explored flux range.

These results imply that water loss during the evolution of super-Earths can remove up to the full 3% water mass fraction assumed in our models for the lowest-mass, most irradiated planets. Since these cases result in complete depletion, our results provide a lower bound on the potential volatile loss: planets with higher initial water contents could plausibly lose even more. However, given that current constraints suggest most super-Earths contain $\lesssim 3 \%$ water by mass (J. G. Rogers et al. 2024), this level of loss may only be relevant for a small subset of the population. In reality, many super-

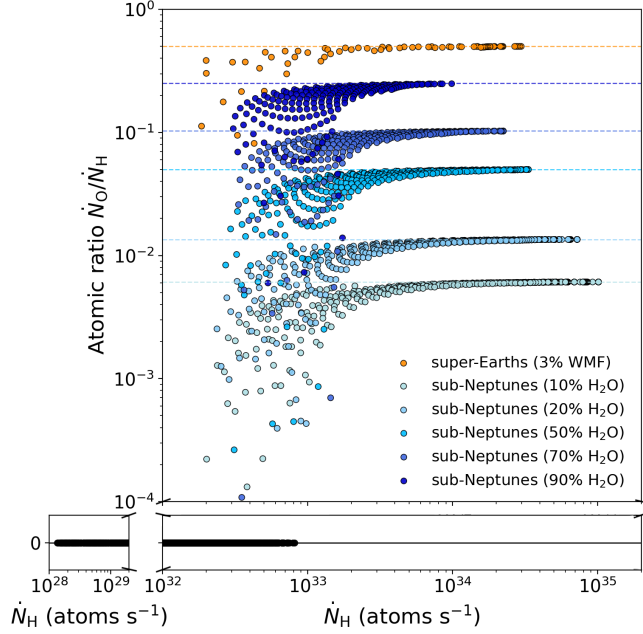


Figure 5. Atomic escape-flux ratio \dot{N}_O/\dot{N}_H for all simulated planets spanning masses $1 - 15M_{\oplus}$, equilibrium temperatures $300 - 2,000$ K, and a wide range of incident F_{XUV} . A denser F_{XUV} sampling was done for the data shown in this plot compared to the previous figures, for better visualization. Cases where oxygen is lost ($x_O \neq 0$) are colored by planetary type and composition as indicated. Dashed lines show the mixing-limited maximum O/H ratios corresponding to each bulk water mass fraction, representing the upper limit for oxygen escape if it occurred at the bulk atmospheric abundance with a $x_O = 1$. Black points at the 0 escape flux ratio line correspond to cases where oxygen is not lost, thus the ratio drops to 0. These cases make up $\sim 75\%$ of the data, overlap with each other, and span approximately 5 orders of magnitude of hydrogen loss (atoms s $^{-1}$).

Earths may be the remnants of sub-Neptune planets that have lost their primordial hydrogen envelopes due to intense stellar irradiation. The evolutionary pathway of these planets likely begins with envelopes that are not purely composed of water vapor but instead contain some amounts of hydrogen. Interestingly, (A. Werlen et al. 2025) suggest that water-dominated envelopes are possible for super-Earths that formed within the ice-line. Such planets may be particularly susceptible to the levels of mass loss we estimate. Their bulk water content is typically limited to a few percent by mass, which is comparable in magnitude to the potential mass loss when the incident XUV fluxes are high.

6.2.2. How much does atmospheric composition change with fractionated loss for sub-Neptunes?

Atmospheric escape does not only remove mass; when the flow fractionates, it can also reshape the composition of the surviving envelope. For sub-Neptunes with mixed

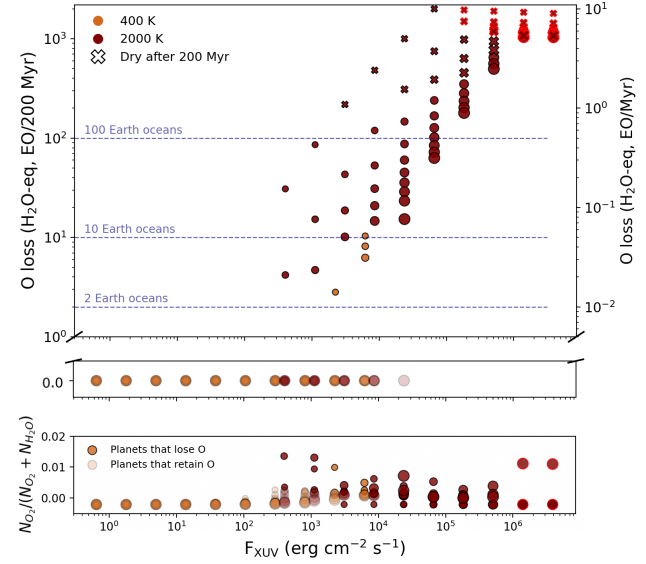


Figure 6. Estimated oxygen-equivalent water loss in Earth oceans for steam atmosphere (3% WMF) super-Earths over 200 Myr (left y-axis) and 1 Myr (right y-axis) as a function of incident XUV flux, assuming constant escape rates over these timespans. Top panel: cases where water is lost due to oxygen loss; middle panel: cases where water is not lost due to oxygen being retained; bottom panel: resulting atmospheric oxygen content after recombination, i.e., oxygen enrichment after mass loss; opaque markers correspond to oxygen-loss cases (top panel), while faint markers correspond to oxygen-retention cases (middle panel). Marker size scales with planetary mass. Red edges indicate planets in the recombination-limited regime.

H_2 - H_2O envelopes, preferential hydrogen loss tends to increase the envelope O/H ratio and therefore its effective metallicity. Here we estimate how efficiently this process can enrich young, warm sub-Neptunes during the post-disk epoch when stellar XUV emission is high.

We consider sub-Neptunes with envelope water mass fraction $Z_{init} = 0.2$ and $T_{eq} = 1,000$ K. At each time step we evaluate the coupled hydrodynamic escape and H-O fractionation solution (Sections 2–4), and update the remaining hydrogen and oxygen reservoirs accordingly. To express the compositional outcome in an intuitive way, we assume that the retained H and O recombine into H_2O (and, when hydrogen becomes limiting, into O-bearing residual gas), and define the instantaneous envelope metallicity as the post-escape water mass fraction in the remaining envelope,

$$Z(t) = \frac{M_{H_2O}(t)}{M_{env}(t)}, \quad (14)$$

where M_{env} is the total surviving envelope mass. This procedure is not a full evolutionary model because we

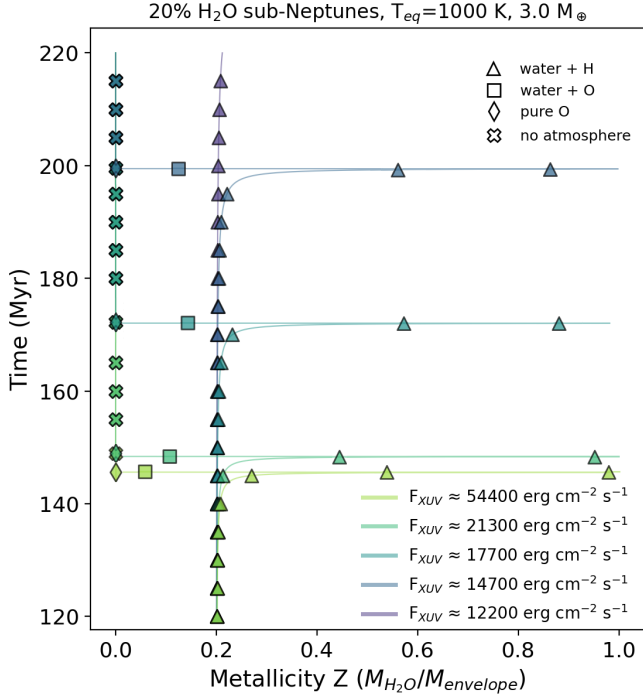


Figure 7. Evolution of the envelope metallicity $Z(t)$ for young sub-Neptunes with initial $Z = 0.2$, $T_{\text{eq}} = 1,000$ K, and $M_p = 3.0 M_{\oplus}$, shown as a function of incident F_{XUV} , over time. Values approaching $Z_{\text{H}_2\text{O}} \simeq 1$ correspond to steam-dominated surviving envelopes.

hold the planetary radius fixed; as a result, the inferred enrichment represents an upper bound

Figures 7–8 illustrate that compositional evolution is strongly threshold dominated. At low irradiation, oxygen is efficiently retained ($x_{\text{O}} \rightarrow 0$), but escape rates are small, so the envelope composition changes only weakly over ~ 200 Myr despite strong microphysical fractionation. At sufficiently high irradiation, escape becomes rapid and oxygen entrainment increases toward $x_{\text{O}} \sim 1$, causing the outflow composition to approach the bulk mixture and reducing the degree of preferential hydrogen loss. Consequently, substantial enrichment requires a narrow intermediate regime: hydrogen escape must be vigorous enough to remove a significant fraction of the envelope, while oxygen must remain at least partially retained long enough for Z to rise.

In the fixed-mass sequence (Fig. 7), enrichment remains negligible below a characteristic XUV threshold, while above it the atmosphere transitions rapidly through successive compositional stages. As hydrogen is removed, the envelope becomes progressively more water rich, approaching $Z \simeq 1$ (a steam-dominated remainder). For the most strongly irradiated cases, continued escape then removes the remaining volatile reservoir on short timescales, so that high- Z phases can be transient

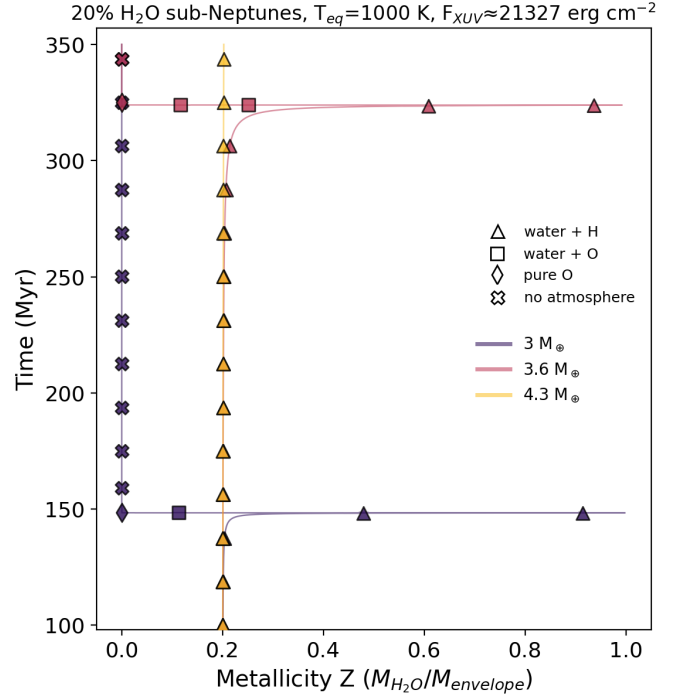


Figure 8. Evolution of the envelope metallicity $Z(t)$ for young sub-Neptunes with initial $Z = 0.2$, $T_{\text{eq}} = 1,000$ K, and $F_{\text{XUV}} = 21,327$, shown as a function of planetary mass, over time. Values approaching $Z_{\text{H}_2\text{O}} \simeq 1$ correspond to steam-dominated surviving envelopes.

and may precede complete atmospheric depletion after a very short pure-oxygen atmosphere state. For a fixed-flux (Fig. 8), the same behavior appears as a strong mass dependence: lower-mass planets evolve through enrichment and depletion much faster, whereas higher-mass sub-Neptunes retain their envelopes longer and exhibit slower or negligible enrichment over 200 Myr.

Our calculations show that fractionated escape can produce substantial water enrichment in young, warm sub-Neptunes as they evolve toward super-Earths. Significant enrichment occurs only for planets that lose most of their primordial H/He envelopes, and it happens rapidly, on timescales of order ~ 10 Myr. Because our estimates represent upper limits on escape efficiency, the enrichment phase is likely more prolonged in reality.

A natural observational signature of this process is a transitional regime populated by increasingly enriched planets as they get closer to the radius valley. This leads to a clear prediction: the bulk of the sub-Neptune population should retain H/He-dominated envelopes with low water mass fractions, as constrained by geochemical considerations (A. Werlen et al. 2025), whereas only planets close or within the radius valley can develop strongly enriched envelopes, potentially transitioning to steam-dominated atmospheres. GJ 9827 d ($1.98 R_{\oplus}$,

$T_{\text{eq}} \sim 620$ K) provides a compelling example. Its location near the radius valley and its inferred high metallicity (x500 times solar, with mass ratio $O/H \approx 4$) are fully consistent with our model predictions for a partially hydrogen-depleted planet sculpted by XUV-driven mass loss (C. Piaulet-Ghorayeb et al. 2024).

7. DISCUSSION

7.1. Comparison to estimated mass loss rates

To validate and contextualize our model, we compare our predicted mass loss rates to previously published values for (well-) characterized exoplanet systems that span a range of atmospheric compositions, sizes, and irradiation levels. We draw comparisons for the 2 extreme cases of atmospheric composition: pure H_2O atmosphere, and pure H/He envelope (approximately 30% helium and 70% hydrogen by mass). We show all results in Table 1.

We begin with the TOI-431 system, which hosts at least three planets, with TOI-431 b and d being of particular interest. TOI-431 b is a short-period super-Earth, while TOI-431 d is a larger sub-Neptune. Observations by A. Osborn et al. (2021) suggest that TOI-431 d likely retains a substantial volatile envelope, which could be either a light H/He layer ($\sim 3.6\%$ by mass) or a heavier water-rich layer ($\sim 33\%$ by mass). To bracket this uncertainty, we compute mass loss rates for both compositions to compare to previous calculations (X. Jiang et al. 2025), as seen in Table 1. In the case of steam, we find that oxygen is strongly retained ($x_O = 0$), potentially enriching the atmosphere as hydrogen escapes. A different scenario holds for TOI-431 b if it has a water envelope ($x_O = 0.87$), underscoring the strong influence of irradiation on escape. While the present-day mass loss rates for the two compositions of TOI-431 d appear comparable, their long-term evolutionary implications diverge significantly: With a H/He envelope, the planet is likely undergoing slow but continuous envelope erosion; in the steam case, the atmosphere is both more tightly bound and composed of heavier volatiles, with hydrogen escaping preferentially and nearly all oxygen being retained. This suggests that a water-rich planet could retain much of its volatile inventory over gigayear timescales, even under moderate XUV flux. As such, TOI-431 d exemplifies how \dot{M} alone is insufficient to constrain atmospheric evolution without knowing the envelope's composition.

We also include the TRAPPIST-1 system, a benchmark for low-mass, rocky, cool exoplanets orbiting an M-dwarf star. We compare our results to the energy-limited escape rates compiled by J. Becker et al. (2020), and recalculate loss rates assuming pure steam atmo-

spheres for all planets. This setup provides insight into whether significant water depletion could occur in the absence of primordial hydrogen, particularly in early outgassed secondary atmospheres. We find that the escape rates reported by J. Becker et al. (2020)—based on energy-limited scalings with fixed heating efficiency and XUV radius equal to the planetary radius—are systematically higher than our results by small factors. We find that escape is strongly fractionating, with hydrogen being preferentially lost while oxygen is retained ($x_O = 0$) for all TRAPPIST planets. If water is the dominant outgassed volatile, our results suggest that TRAPPIST-1 planets could evolve toward oxygen-rich atmospheres, with the ultimate outcome depending on the efficiency of surface sinks in removing excess oxygen. While we observe the same trend as J. Becker et al. (2020) in decreasing XUV flux and mass loss rate with orbital distance, the systematically lower rates highlight the need for composition- and regime-aware models in assessing long-term atmospheric evolution for terrestrial planets.

Moreover, we apply our mass loss framework to three additional systems: K2-18 b, a sub-Neptune candidate, and HD 63433 c, a young sub-Neptune. For K2-18 b, we run our models both for a pure H/He case (no fractionation) and for a pure water composition (fully fractionated) to bracket the possible extremes. Our predicted escape rates are lower by approximately an order of magnitude, for both compositions, compared to the estimate from L. A. d. Santos et al. (2020), who applied an energy-limited model based on partial Lyman- α transit data. We emphasize that the true escape rates are expected to lie between our two bracketing cases, given the range of possible atmospheric compositions of K2-18 b.

For HD 63433 c, we find that BOREAS predicts escape rates approximately an order of magnitude lower than the value reported by M. Zhang et al. (2022). Given the youth and activity of the host star, part of the observed helium signal may also arise from stellar variability.

In general, pure steam atmospheres yield lower \dot{M} values than equivalent pure H/He envelopes, due to their higher mean molecular weight and lower scale heights. Our results highlight the importance of composition-sensitive modeling frameworks for interpreting present-day escape and volatile retention. While our estimates differ quantitatively from literature values, these variations are expected due to differences in assumed opacity, heating efficiency, and hydrodynamic structure, . Importantly, our results reinforce the need for composition-dependent models when interpreting atmospheric evolution across exoplanet populations.

Table 1. Mass loss rate comparison for different exoplanets. In our comparisons, we assume either a pure steam or pure H/He atmosphere. The F_{XUV} values and mass loss rates are static and correspond to present-day conditions; comparisons are intended to be illustrative rather than evolutionary.

Planet	F_{XUV} [erg cm $^{-2}$ s $^{-1}$]	Previous Mass Loss rates [g/s]	This Study (Fractionated H ₂ O Atmosphere) [g/s]	This Study (H/He Envelope, no fractionation) [g/s]
TOI-431 b	70,286 ^[a]	$10^{10.51}$ ^[a]	$10^{9.972}$	No convergence
TOI-431 d	93 ^[a]	$10^{9.140}$ ^[a]	$10^{8.742}$	$10^{9.122}$
TRAPPIST-1 b	2,935 ^[b]	$8.29 \cdot 10^8$ ^[b]	$5.074 \cdot 10^8$	-
TRAPPIST-1 c	1,565 ^[b]	$3.62 \cdot 10^8$ ^[b]	$2.663 \cdot 10^8$	-
TRAPPIST-1 d	788 ^[b]	$2.61 \cdot 10^8$ ^[b]	$1.731 \cdot 10^8$	-
TRAPPIST-1 e	456 ^[b]	$9.08 \cdot 10^7$ ^[b]	$8.799 \cdot 10^7$	-
TRAPPIST-1 f	264 ^[b]	$6.58 \cdot 10^7$ ^[b]	$4.767 \cdot 10^7$	-
TRAPPIST-1 g	178 ^[b]	$4.78 \cdot 10^7$ ^[b]	$3.140 \cdot 10^7$	-
TRAPPIST-1 h	102 ^[b]	$2.90 \cdot 10^7$ ^[b]	$2.370 \cdot 10^7$	-
K2-18 b	107.9 ^[c]	$3.50 \cdot 10^8$ ^[c]	$2.522 \cdot 10^7$	$3.279 \cdot 10^7$
HD 63433 c	6,000	$2.1 \cdot 10^{10}$ ^[d]	$1.249 \cdot 10^9$	$1.860 \cdot 10^9$
TOI 560 b	5,000 ^[e]	$1.61 \cdot 10^{11}$ ^[e]	$1.740 \cdot 10^9$	$3.885 \cdot 10^9$
TOI 1430.01	6,800 ^[e]	$1.32 \cdot 10^{11}$ ^[e]	$1.495 \cdot 10^9$	$4.331 \cdot 10^9$
TOI 1683.01	12,000 ^[e]	$2.48 \cdot 10^{10}$ ^[e]	$3.057 \cdot 10^9$	$1.008 \cdot 10^{10}$
TOI 2076 b	6,000 ^[e]	$2.43 \cdot 10^{10}$ ^[e]	$2.787 \cdot 10^9$	$7.204 \cdot 10^9$

^a After X. Jiang et al. (2025).

^b After J. Becker et al. (2020).

^c After L. A. d. Santos et al. (2020).

^d After M. Zhang et al. (2022).

^e After M. Zhang et al. (2023).

7.2. Simplifications and Caveats

Several assumptions and simplifications are inherent in our model framework:

- We assume sufficient XUV energy to fully dissociate H₂ and H₂O molecules into atomic hydrogen and/or oxygen, neglecting partial dissociation or altitude-dependent dissociation scenarios. This is left for future work but could modestly alter c_s and other parameters, that affecting both the total mass loss rate as well as the fractionated fluxes of different species.
- Accumulated oxygen in the upper atmosphere could potentially shield deeper atmospheric layers or introduce radiative cooling effects, altering escape rates over time (A. Nakayama et al. 2022; Y. Kawamura et al. 2024; T. Yoshida et al. 2024; W. Broussard et al. 2025). We do not currently model this effect.
- We assume an isothermal base at T_{eq} up to R_{XUV} . In reality, in very hot or thin atmospheres, the base might already heat up or expand beyond the nominal “radiative-convective” boundary.
- We do not model recombination or ionization reactions (e.g., hydrogen and oxygen recombining into water) within the outflow region. Instead, we focus on instantaneous fractionation under the assumption of stable photodissociation conditions.
- We ignore helium fractionation; in practice, the model can be adapted to 3-species fractionation for H, O, and He, but this falls outside the scope of the current study. When looking at mixed atmospheres, we model H₂ mixed with H₂O.
- Our water loss estimates in Section 6.2 are based on a constant extrapolation of instantaneous escape rates over 200 Myr. In reality, as hydrogen is depleted and the envelope becomes increasingly oxygen-rich, mass loss rates may decline due to rising mean molecular weight, reduced scale height, or even the onset of diffusion-limited es-

cape. Consequently, the net atmospheric evolution remains uncertain, and resolving it requires fully coupled interior–atmosphere–escape models within a self-consistent evolutionary framework.

- If hydrogen becomes a trace species in a heavy oxygen-rich atmosphere, its escape may become diffusion-limited: H atoms must diffuse upward through a heavier background before they can escape, throttling the hydrogen loss rate. We do not model this regime in this study.

8. CONCLUSIONS

This study aimed to investigate how hydrodynamic atmospheric escape driven by stellar XUV not only removes atmospheric mass from planets, but also alters the chemical composition of their atmospheres through fractionation. In particular, we focused on the differential escape of hydrogen and oxygen in steam and mixed-composition atmospheres of super-Earths and sub-Neptunes, and explored the implications for planetary evolution.

To achieve this, we developed an open-source, self-consistent, coupled atmospheric escape-fractionation model called BOREAS. Our framework built on hydrodynamic mass loss calculations that span both energy-limited and recombination-limited regimes and incorporate a mass-dependent escape prescription that tracks the partitioning of hydrogen and oxygen fluxes. We validated our results against benchmark planets with published mass loss estimates and applied the model to a broad parameter space spanning planet mass, radius, equilibrium temperature, age, and incident XUV flux. Overall, we demonstrated that atmospheric escape is not just a bulk erosion process, but also involves a fractionation process that can change planetary compositions over time. Understanding the coupled dynamics of mass loss and fractionation is important for interpreting the nature of exoplanets, especially those with atmospheres interpreted to be water-rich: they may have originated from initially water-poor, H/He-dominated compositions and become H-depleted and water-rich during their fractionated mass loss histories. This is particularly relevant for planets within or near the radius valley; GJ 9827 d and its possible inferred steam atmosphere (C. Piaulet-Ghorayeb et al. 2024) is a perfect example. Future extensions of this work may incorporate time-dependent thermal evolution and coupled radius contraction to fully capture the interplay between atmospheric loss, composition, and structure across planetary lifetimes.

Our key findings are as follows:

1. Oxygen is typically retained: Across most of our parameter space, hydrogen escapes more readily than oxygen. The oxygen fractionation factor $x_O = 0$ in these cases, and remains < 1 for most super-Earths and sub-Neptunes, implying negligible oxygen escape—except under the most extreme irradiation or low-gravity conditions where it approaches unity.
2. Mass loss is composition-dependent: For the same planet mass, pure H/He atmospheres will most likely lose mass at significantly higher rates than pure steam atmospheres, due to their lower mean molecular weight and larger scale heights. Models that neglect composition effects may overestimate escape rates. This is evident in nearly all of our modeled escape rates for the benchmarked planets, where results vary by orders of magnitude depending on assumed atmospheric composition. In turn, this implies that observed mass-loss rates provide a powerful diagnostic of atmospheric composition, as different compositions produce an observable imprint on the inferred loss rates (J. G. Rogers et al. 2026).
3. Fractionated escape may enrich atmospheres in water: Sub-Neptunes with modest water abundances (10–20%, equivalent to initial metallicity $Z = 0.1–0.2$) can become water-dominated, steam worlds, or oxygen worlds over 200 Myr due to preferential hydrogen loss, but only when oxygen is also entrained in the flow. Thus, this enrichment operates only over a limited evolutionary window, applying primarily to low-mass sub-Neptunes experiencing intense irradiation, where oxygen remains entrained in the outflow. We therefore predict that such compositional transformations are most relevant for planets near or within the radius valley, where a residual atmosphere is retained while the majority of hydrogen has been preferentially lost to space.

ACKNOWLEDGMENTS

C.D. acknowledges support from the Swiss National Science Foundation under grant TMSGI2_211313 and the COPL project funding for Evolution and Diversity of Super-Earth Atmospheres. This work has been carried out within the framework of the NCCR PlanetS supported by the Swiss National Science Foundation under grant 51NF40_205606. J.E.O is supported by a Royal Society University Research Fellowship. This project

has received funding from the European Research Council (ERC) under the European Union’s Horizon 2020 research and innovation programme (Grant agreement No. 853022). We thank the anonymous reviewers for their insightful comments, which greatly helped to improve this study. We acknowledge the use of large lan-

guage models (LLMs), including ChatGPT, to improve the grammar, clarity, and readability of the manuscript.

Software: The package developed for this project is publicly available under a custom license and can be found in <https://github.com/ExoInteriors/BOREAS>.

APPENDIX

A. ATMOSPHERIC ESCAPE MODEL

A.1. *Hydrodynamic Escape Equations*

$$\rho_{\text{XUV}} = \rho_{\text{photo}} \exp \left[\frac{GM_p}{c_s^2} \left(\frac{1}{R_{\text{XUV}}} - \frac{1}{R_p} \right) \right], \quad (\text{A1})$$

where ρ_{photo} is determined from the balance between gravity and radiative opacity at the base (e.g. $\rho_{\text{photo}} \sim g/(\kappa_{IR} c_s^2)$), G is the gravitational constant, M_p the planet mass, , and c_s the sound speed in this (near-)isothermal region.

Above R_{XUV} , the atmosphere is further heated by XUV radiation and the flow accelerates into a supersonic wind. Here the velocity structure is determined by solving the isothermal Parker wind equations. In our implementation, the sonic point is defined as

$$R_s = \frac{GM_p}{2c_s^2}, \quad (\text{A2})$$

and its relation to R_{XUV} dictates which branch of the Parker wind solution is used:

- If $R_s \geq R_{\text{XUV}}$, the standard Parker wind solution is used,
- If $R_s < R_{\text{XUV}}$, a modified solution with a constant parameter is adopted to ensure consistency with the subsonic base.

$$C = 1 - 4 \ln \left(\frac{R_{\text{XUV}}}{R_s} \right) - \frac{4R_s}{R_{\text{XUV}}}, \quad (\text{A3})$$

$$\rho_{\text{shape}}(r) = \left(\frac{R_s}{r} \right)^2 \left(\frac{c_s}{u(r)} \right), \quad (\text{A4})$$

$$\tau(R_{\text{XUV}}) = \int_{R_{\text{XUV}}}^{\infty} \rho(r) \chi_{\text{XUV}} dr, \quad (\text{A5})$$

$$\tau_{\text{geom}} \equiv \int_{R_{\text{XUV}}}^{\infty} \rho_{\text{shape}}(r) dr, \quad (\text{A6})$$

$$\rho_{\text{XUV}} = \frac{1}{\chi_{\text{XUV}} \tau_{\text{geom}}}. \quad (\text{A7})$$

$$\dot{M} = 4\pi R_{\text{XUV}}^2 \rho_{\text{XUV}} u(R_{\text{XUV}}). \quad (\text{A8})$$

B. ATMOSPHERIC MASS FRACTIONATION

B.1. *Fractionation Factor Derivation*

$$\phi_O = \phi_H f_O x_O, \quad (B9)$$

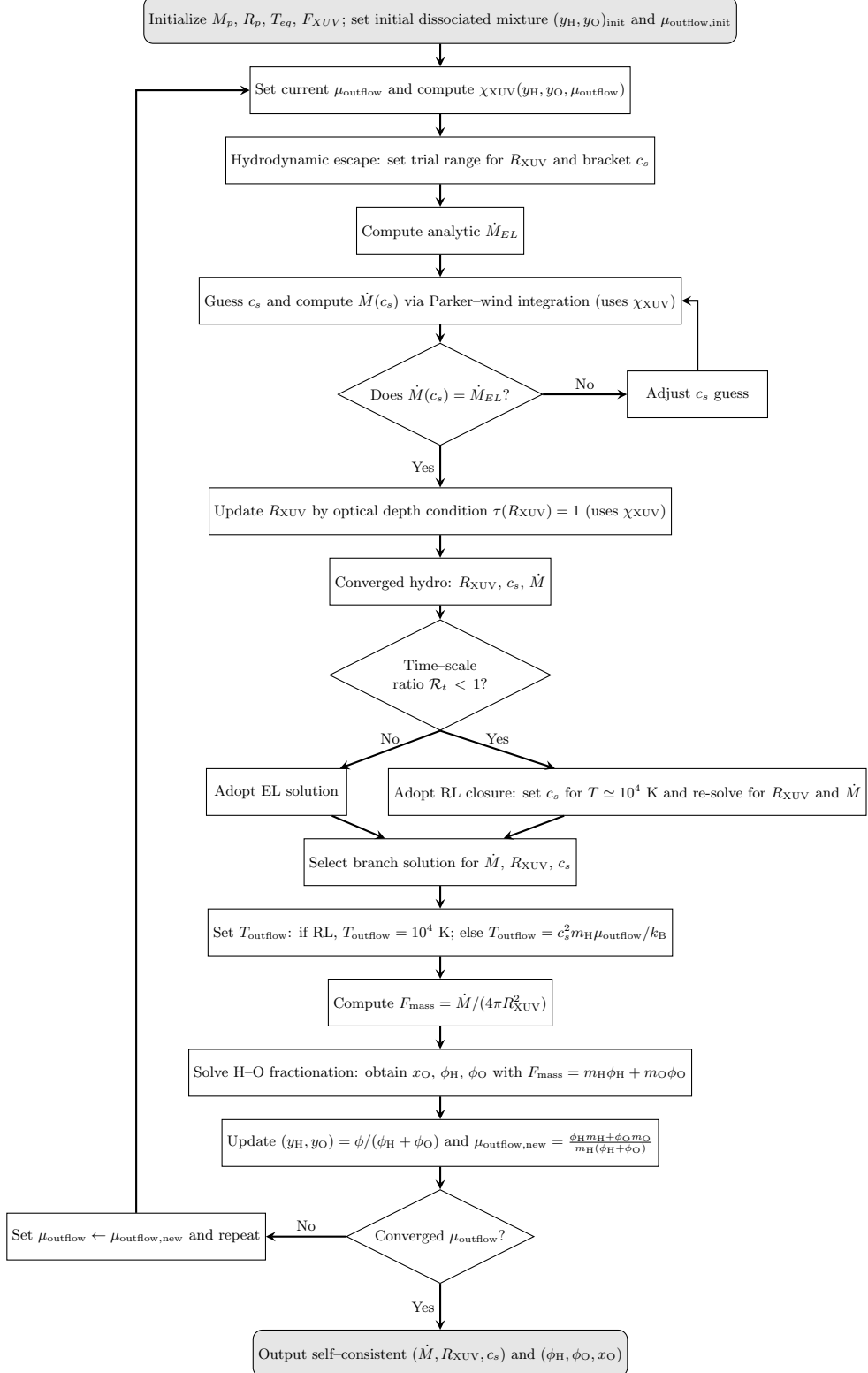
$$x_O = 1 - \frac{g (m_O - m_H) b_{HO}(T_{outflow})}{k_B T_{outflow} \phi_H (1 + f_O)}, \quad (B10)$$

The outflow temperature used in the diffusion coefficient is

$$T_{outflow} = \begin{cases} 10^4 \text{ K}, & (\text{RL}) \\ \frac{c_s^2 m_H \mu_{outflow}}{k_B}, & (\text{EL}). \end{cases} \quad (B11)$$

C. FLOWCHART OF THE BOREAS FRAMEWORK

Figure 9. Flowchart for the coupled hydrodynamic escape and H–O fractionation model. The outer loop iterates on μ_{outflow} (and thus the atomic mixture used for χ_{XUV}) to obtain a self-consistent R_{XUV} , c_s , \dot{M} , and $(\phi_{\text{H}}, \phi_{\text{O}})$. EL: energy-limited; RL: recombination-limited.



REFERENCES

Baraffe, I., Homeier, D., Allard, F., & Chabrier, G. 2015, *Astronomy & Astrophysics*, 577, A42, doi: [10.1051/0004-6361/201425481](https://doi.org/10.1051/0004-6361/201425481)

Bean, J. L., Raymond, S. N., & Owen, J. E. 2021, *Journal of Geophysical Research: Planets*, 126, e2020JE006639, doi: [10.1029/2020JE006639](https://doi.org/10.1029/2020JE006639)

Becker, J., Gallo, E., Hodges-Kluck, E., Adams, F. C., & Barnes, R. 2020, *The Astronomical Journal*, 159, 275, doi: [10.3847/1538-3881/ab8fb0](https://doi.org/10.3847/1538-3881/ab8fb0)

Broussard, W., Schwieterman, E. W., Sousa-Silva, C., et al. 2025, The Impact of Extended CO₂ Cross Sections on Temperate Anoxic Planet Atmospheres, arXiv, doi: [10.48550/arXiv.2501.08434](https://doi.org/10.48550/arXiv.2501.08434)

Burn, R., Bali, K., Dorn, C., Luque, R., & Grimm, S. L. 2024, Water-rich sub-Neptunes and rocky super Earths around different Stars: Radii shaped by Volatile Partitioning, Formation, and Evolution, arXiv, doi: [10.48550/arXiv.2411.16879](https://doi.org/10.48550/arXiv.2411.16879)

Cherubim, C., Wordsworth, R., Bower, D., et al. 2025, An Oxidation Gradient Straddling the Small Planet Radius Valley, arXiv, doi: [10.48550/arXiv.2503.05055](https://doi.org/10.48550/arXiv.2503.05055)

Cherubim, C., Wordsworth, R., Hu, R., & Shkolnik, E. 2024, Strong fractionation of deuterium and helium in sub-Neptune atmospheres along the radius valley, arXiv, doi: [10.48550/arXiv.2402.10690](https://doi.org/10.48550/arXiv.2402.10690)

Dorn, C., Khan, A., Heng, K., et al. 2015, *Astronomy & Astrophysics*, 577, A83

Dorn, C., Venturini, J., Khan, A., et al. 2017, *Astronomy & Astrophysics*, 597, A37, doi: [10.1051/0004-6361/201628708](https://doi.org/10.1051/0004-6361/201628708)

Eylen, V. V., Astudillo-Defru, N., Bonfils, X., et al. 2021, *Monthly Notices of the Royal Astronomical Society*, stab2143, doi: [10.1093/mnras/stab2143](https://doi.org/10.1093/mnras/stab2143)

Ginzburg, S., Schlichting, H. E., & Sari, R. 2018, *Monthly Notices of the Royal Astronomical Society*, 476, 759, doi: [10.1093/mnras/sty290](https://doi.org/10.1093/mnras/sty290)

Guillot, T. 2010, On the radiative equilibrium of irradiated planetary atmospheres, doi: [10.1051/0004-6361/200913396](https://doi.org/10.1051/0004-6361/200913396)

Hunten, D. M., Pepin, R. O., & Walker, J. C. G. 1987, *Icarus*, 69, 532, doi: [10.1016/0019-1035\(87\)90022-4](https://doi.org/10.1016/0019-1035(87)90022-4)

Jiang, X., Jiang, J. H., Burn, R., & Zhu, Z.-H. 2025, *The Astrophysical Journal*, 980, 175, doi: [10.3847/1538-4357/ada607](https://doi.org/10.3847/1538-4357/ada607)

Jin, S., Mordasini, C., Parmentier, V., et al. 2014, *The Astrophysical Journal*, 795, 65, doi: [10.1088/0004-637X/795/1/65](https://doi.org/10.1088/0004-637X/795/1/65)

Kawamura, Y., Yoshida, T., Terada, N., et al. 2024, *The Astrophysical Journal*, 967, 95, doi: [10.3847/1538-4357/ad3e7e](https://doi.org/10.3847/1538-4357/ad3e7e)

Kubyshkina, D., Fossati, L., Erkaev, N. V., et al. 2018, *Astronomy & Astrophysics*, 619, A151, doi: [10.1051/0004-6361/201833737](https://doi.org/10.1051/0004-6361/201833737)

Lammer, H., Kasting, J. F., Chassefière, E., et al. 2008, in *Comparative Aeronomy*, ed. A. F. Nagy, A. Balogh, T. E. Cravens, M. Mendillo, & I. Mueller-Wodarg (New York, NY: Springer), 399–436, doi: [10.1007/978-0-387-87825-6_11](https://doi.org/10.1007/978-0-387-87825-6_11)

Lammer, H., Selsis, F., Ribas, I., et al. 2003, *The Astrophysical Journal*, 598, L121, doi: [10.1086/380815](https://doi.org/10.1086/380815)

Lopez, E. D., Fortney, J. J., & Miller, N. 2012, *The Astrophysical Journal*, 761, 59, doi: [10.1088/0004-637X/761/1/59](https://doi.org/10.1088/0004-637X/761/1/59)

Loyd, R. O. P., Shkolnik, E. L., Schneider, A. C., et al. 2020, *The Astrophysical Journal*, 890, 23, doi: [10.3847/1538-4357/ab6605](https://doi.org/10.3847/1538-4357/ab6605)

Luger, R., & Barnes, R. 2015, *Astrobiology*, 15, 119, doi: [10.1089/ast.2014.1231](https://doi.org/10.1089/ast.2014.1231)

Luo, H., Dorn, C., & Deng, J. 2024, Majority of water hides deep in the interiors of exoplanets, arXiv, doi: [10.48550/arXiv.2401.16394](https://doi.org/10.48550/arXiv.2401.16394)

Madhusudhan, N., Sarkar, S., Constantinou, S., et al. 2023, *The Astrophysical Journal Letters*, 956, L13, doi: [10.3847/2041-8213/acf577](https://doi.org/10.3847/2041-8213/acf577)

Mordasini, C. 2020, Planetary evolution with atmospheric photoevaporation I. Analytical derivation and numerical study of the evaporation valley and transition from super-Earths to sub-Neptunes, doi: [10.1051/0004-6361/201935541](https://doi.org/10.1051/0004-6361/201935541)

Murray-Clay, R. A., Chiang, E. I., & Murray, N. 2009, *The Astrophysical Journal*, 693, 23–42, doi: [10.1088/0004-637x/693/1/23](https://doi.org/10.1088/0004-637x/693/1/23)

Nakayama, A., Ikoma, M., & Terada, N. 2022, *The Astrophysical Journal*, 937, 72, doi: [10.3847/1538-4357/ac86ca](https://doi.org/10.3847/1538-4357/ac86ca)

Odert, P., Lammer, H., Erkaev, N. V., et al. 2018, *Icarus*, 307, 327, doi: [10.1016/j.icarus.2017.10.031](https://doi.org/10.1016/j.icarus.2017.10.031)

Osborn, A., Armstrong, D. J., Cale, B., et al. 2021, *Monthly Notices of the Royal Astronomical Society*, 507, 2782, doi: [10.1093/mnras/stab2313](https://doi.org/10.1093/mnras/stab2313)

Osterbrock, D. E., & Ferland, G. J. 2006, *Astrophysics of gaseous nebulae and active galactic nuclei*

Owen, J. E. 2019, *Annual Review of Earth and Planetary Sciences*, 47, 67, doi: [10.1146/annurev-earth-053018-060246](https://doi.org/10.1146/annurev-earth-053018-060246)

Owen, J. E., & Alvarez, M. A. 2015, The Astrophysical Journal, 816, 34, doi: [10.3847/0004-637X/816/1/34](https://doi.org/10.3847/0004-637X/816/1/34)

Owen, J. E., & Jackson, A. P. 2012, Monthly Notices of the Royal Astronomical Society, 425, 2931, doi: [10.1111/j.1365-2966.2012.21481.x](https://doi.org/10.1111/j.1365-2966.2012.21481.x)

Owen, J. E., & Schlichting, H. E. 2024, MNRAS, 528, 1615, doi: [10.1093/mnras/stad3972](https://doi.org/10.1093/mnras/stad3972)

Owen, J. E., & Wu, Y. 2016, The Astrophysical Journal, 817, 107, doi: [10.3847/0004-637X/817/2/107](https://doi.org/10.3847/0004-637X/817/2/107)

Owen, J. E., & Wu, Y. 2017, The Astrophysical Journal, 847, 29, doi: [10.3847/1538-4357/aa890a](https://doi.org/10.3847/1538-4357/aa890a)

Piaulet-Ghorayeb, C., Benneke, B., Radica, M., et al. 2024, The Astrophysical Journal Letters, 974, L10, doi: [10.3847/2041-8213/ad6f00](https://doi.org/10.3847/2041-8213/ad6f00)

Rogers, J. G., Dorn, C., Raj, V. A., Schlichting, H. E., & Young, E. D. 2024, Most Super-Earths Have Less Than 3% Water, arXiv, doi: [10.48550/arXiv.2409.17394](https://doi.org/10.48550/arXiv.2409.17394)

Rogers, J. G., Gupta, A., Owen, J. E., & Schlicdornhting, H. E. 2021, Monthly Notices of the Royal Astronomical Society, 508, 5886, doi: [10.1093/mnras/stab2897](https://doi.org/10.1093/mnras/stab2897)

Rogers, J. G., Owen, J. E., Schreyer, E., & Kirk, J. 2026, arXiv preprint arXiv:2601.14254

Santos, L. A. d., Ehrenreich, D., Bourrier, V., et al. 2020, Astronomy & Astrophysics, 634, L4, doi: [10.1051/0004-6361/201937327](https://doi.org/10.1051/0004-6361/201937327)

Seager, S. 2010, Exoplanet Atmospheres: Physical Processes. By Sara Seager. Princeton University Press, 2010. ISBN: 978-1-4008-3530-0

Storey, P. J., & Hummer, D. G. 1995, Mon. Not. R. Astron. Soc., 272, 41

Tian, F. 2015, Annual Review of Earth and Planetary Sciences, 43, 459, doi: [10.1146/annurev-earth-060313-054834](https://doi.org/10.1146/annurev-earth-060313-054834)

Verner, D. A., Ferland, G. J., Korista, K. T., & Yakovlev, D. G. 1996, Astrophys. J., 465, 487

Werlen, A., Dorn, C., Burn, R., et al. 2025, Sub-Neptunes Are Drier Than They Seem: Rethinking the Origins of Water-Rich Worlds, arXiv, doi: [10.48550/arXiv.2507.00765](https://doi.org/10.48550/arXiv.2507.00765)

Yoshida, T., Terada, N., & Kuramoto, K. 2024, Suppression of hydrodynamic escape of an H₂-rich early Earth atmosphere by radiative cooling of carbon oxides, arXiv, doi: [10.48550/arXiv.2411.15456](https://doi.org/10.48550/arXiv.2411.15456)

Zahnle, K., Kasting, J. F., & Pollack, J. B. 1990, Icarus, 84, 502, doi: [10.1016/0019-1035\(90\)90050-J](https://doi.org/10.1016/0019-1035(90)90050-J)

Zahnle, K. J., & Kasting, J. F. 1986, Icarus, 68, 462, doi: [10.1016/0019-1035\(86\)90051-5](https://doi.org/10.1016/0019-1035(86)90051-5)

Zhang, M., Knutson, H. A., Dai, F., et al. 2023, Astron. J., 165, 62

Zhang, M., Knutson, H. A., Wang, L., et al. 2022, The Astronomical Journal, 163, 68, doi: [10.3847/1538-3881/ac3f3b](https://doi.org/10.3847/1538-3881/ac3f3b)